5. C. J. Kloxin, T. F. Scott, B. J. Adzima, C. N. Bowman, *Macromolecules* **43**, 2643 (2010).
6. R. J. Wojtecki, M. A. Meador, S. J. Rowan, *Nat. Mater.* **10**, 14 (2011).
7. M. S. Green, A. V. Tobolsky, *J. Chem. Phys.* **14**, 80 (1946).
8. M. Rubinstein, A. N. Semenov, *Macromolecules* **31**, 1386 (1998).
9. F. Tanaka, *Polymer Physics: Applications to Molecular Association and Thermoreversible Gelation* (Cambridge Univ. Press, Cambridge, 2011).
10. L. Leibler, M. Rubinstein, R. H. Colby, *J. Phys. II* **3**, 1581 (1993).
11. T. F. Scott, A. D. Schneider, W. D. Cook, C. N. Bowman, *Science* **308**, 1615 (2005).
12. Y. Higaki, H. Otsuka, A. Takahara, *Macromolecules* **39**, 2121 (2006).
13. R. Nicolaÿ, J. Kamada, A. van Wassen, K. Matyjaszewski, *Macromolecules* **43**, 4355 (2010).
14. H. Y. Park, C. J. Kloxin, T. F. Scott, C. N. Bowman, *Macromolecules* **43**, 10188 (2010).
15. B. Ghosh, M. W. Urban, *Science* **323**, 1458 (2009).
16. Y. Amamoto, J. Kamada, H. Otsuka, A. Takahara, K. Matyjaszewski, *Angew. Chem. Int. Ed.* **50**, 1660 (2011).
17. X. X. Chen *et al.*, *Science* **295**, 1698 (2002).
18. B. J. Adzima, H. A. Aguirre, C. J. Kloxin, T. F. Scott, C. N. Bowman, *Macromolecules* **41**, 9112 (2008).
19. Y. Zhang, A. A. Broekhuis, F. Picchioni, *Macromolecules* **42**, 1906 (2009).
20. P. Reutenauer, E. Buhler, P. J. Boul, S. J. Candau, J. M. Lehn, *Chemistry* **15**, 1893 (2009).
21. R. V. Kudryavtsev, D. N. Kursanov, *Zhurnal Obshchei Khimii* **27**, 1686 (1957).
22. J. Otera, *Chem. Rev.* **93**, 1449 (1993).
23. C. A. May, Ed., *Epoxy Resins: Chemistry and Technology* (Dekker, New York, 1988).
24. R. T. Deam, S. F. Edwards, *Philos. Trans. R. Soc. A* **280**, 317 (1976).
25. J. C. Dyre, *Rev. Mod. Phys.* **78**, 953 (2006).
26. C. A. Angell, *Science* **267**, 1924 (1995).
27. G. Urbain, Y. Bottinga, P. Richet, *Geochim. Cosmochim. Acta* **46**, 1061 (1982).
28. D. J. Plazek, V. M. O'Rourke, *J. Polym. Sci. A2 Polym. Phys.* **9**, 209 (1971).
29. D. J. Plazek, C. A. Bero, I. C. Chay, *J. Non-Cryst. Solids* **172–174**, 181 (1994).

Acknowledgments: We gratefully acknowledge helpful discussions, with H. A. H. Meijer and A. J. Ryan on polymer processing, with K. Matyjaszewski on chemical reactions and catalysis, and with F. Krzakala and A. Maggs on glass transition. We are indebted to L. Breucker and S. Abadie for help with experiments. We acknowledge funding from ESPCI, CNRS and Arkema. The authors are declared to be inventors on three patents filed by CNRS related to the work presented here: L. Leibler, D. Montarnal, F. Tournilhac, M. Capelot, FR10.54213 (2010); FR11.50888 (2011); and FR11.50546 (2011).

Supporting Online Material
www.sciencemag.org/cgi/content/full/334/6058/965/DC1
Materials and Methods
Figs. S1 to S13
Table S1
Movie S1

15 August 2011; accepted 5 October 2011
10.1126/science.1212648

Domain Dynamics During Ferroelectric Switching

Christopher T. Nelson,[1] Peng Gao,[1] Jacob R. Jokisaari,[1] Colin Heikes,[2] Carolina Adamo,[2] Alexander Melville,[2] Seung-Hyub Baek,[3] Chad M. Folkman,[3] Benjamin Winchester,[4] Yijia Gu,[4] Yuanming Liu,[5] Kui Zhang,[1] Enge Wang,[6] Jiangyu Li,[5] Long-Qing Chen,[4] Chang-Beom Eom,[3] Darrell G. Schlom,[2,7] Xiaoqing Pan[1]*

The utility of ferroelectric materials stems from the ability to nucleate and move polarized domains using an electric field. To understand the mechanisms of polarization switching, structural characterization at the nanoscale is required. We used aberration-corrected transmission electron microscopy to follow the kinetics and dynamics of ferroelectric switching at millisecond temporal and subangstrom spatial resolution in an epitaxial bilayer of an antiferromagnetic ferroelectric ($BiFeO_3$) on a ferromagnetic electrode ($La_{0.7}Sr_{0.3}MnO_3$). We observed localized nucleation events at the electrode interface, domain wall pinning on point defects, and the formation of ferroelectric domains localized to the ferroelectric and ferromagnetic interface. These results show how defects and interfaces impede full ferroelectric switching of a thin film.

Ferroelectric materials have numerous applications, including high-density and nonvolatile memories (*1*–*3*) and a broad range of electronic, optical, and acoustic devices (*2*). The utility of ferroelectrics is derived from a reversible transition between equivalent polar orientation states under an applied electric field and from that transition's coupling to other material properties including strain (*4*, *5*), magnetic order (*6*), and surface charge (*7*). Most of these applications require low-dimensional geometries such as thin films and deterministic control of the local polarization state at the interface (*8*). Thus, it is critical to understand the process of polarization switching in epitaxial thin films.

In this work, we studied the domain nucleation and evolution during switching of a ferroelectric $BiFeO_3$ thin film, using in situ structural characterization by transmission electron microscopy (TEM). Polarization switching is induced by an applied electric field oriented along the film normal between a surface probe and a planar bottom electrode, the same geometry used for surface probe characterization depicted schematically in Fig. 1. Ferroelectric switching occurs through a process of inhomogenous nucleation and anisotropic growth of favorably oriented domains (*9*). In this geometry, it is typically modeled by a single nucleation event occurring at the probe contact with the film surface, the maximum of the applied field, followed by rapid propagation of the nucleated domain across the film and slow lateral growth (see simulation in fig. S1 and movie S1). The creep-type lateral expansion stage is well known for switching in thin films from surface probe measurements (*10*) and modeling (*11*); however, experimental observations of the initial normal-axis growth process are absent except at much larger length scales (*12*, *13*). In this work, we followed domain nucleation and evolution in cross-section and directly observed inhomogeneous nucleation events, domain wall pinning, and the formation of ferroelectric domains localized at interfaces.

Local switching of a 100-nm $(001)_P$ oriented $BiFeO_3$ ferroelectric film was performed by applying an electrical bias between an etched tungsten surface probe and a 20-nm $La_{0.7}Sr_{0.3}MnO_3$ buffer electrode. This bilayer was grown on closely lattice-matched single-crystal $(110)_O$ $TbScO_3$ substrates (compressive strain <0.14%) to avoid instabilities from epitaxial strain (*14*) and misfit dislocations (*15*) or flexoelectric effects from strain gradients (*16*) (O indicates orthorhombic indices and P indicates pseudocubic, where $[110]_O \parallel [001]_P$). The bias between the surface probe and buffer electrode results in an inhomogenous out-of-plane electric field in the $BiFeO_3$ film, promoting a transition among the eight possible $<111>_P$ polarization directions between the four "up" and four "down" orientation states. Three types of switching are possible, classified by the angular rotation of the polarization vector during swiching: 71°, 109°, or 180°. We find that the preferred switching path is the 71° rotation of the spontaneous polarization by the reversal of only the polarization component parallel to the applied field, in this case the film normal (*z* axis), in agreement with other studies (*17*–*19*). Piezoresponse force microscopy (PFM) indicates that the as-grown $BiFeO_3$ films are predominantly upward-poled. Figure 1A shows an out-of-plane PFM phase image from a 100-nm $BiFeO_3$ film, which was locally switched by a positive probe bias of 20.6 V with a 2-s dwell time, producing a downward-poled domain ~400 nm in diameter.

Diffraction contrast TEM was used to resolve the evolution of the domain structure along the depth of the film in situ. A cross-section of the 100-nm $BiFeO_3$ film measured by PFM was

[1]Department of Materials Science and Engineering, University of Michigan, Ann Arbor, MI 48109, USA. [2]Department of Materials Science and Engineering, Cornell University, Ithaca, NY 14853, USA. [3]Department of Materials Science and Engineering, University of Wisconsin–Madison, Madison, WI 53706, USA. [4]Department of Materials Science and Engineering, Penn State University, University Park, PA 16802, USA. [5]Department of Mechanical Engineering, University of Washington, Seattle, WA 98195, USA. [6]School of Physics, Peking University, Beijing 100871, China. [7]Kavli Institute at Cornell for Nanoscale Science, Ithaca, NY 14853, USA.

*To whom correspondence should be addressed. E-mail: panx@umich.edu

Downloaded from www.sciencemag.org on November 17, 2011

thinned to electron transparency, ~60 nm in thickness (fig. S2), and biased between the tungsten probe in contact with the film surface and the grounded $La_{0.7}Sr_{0.3}MnO_3$ bottom electrode. The sample geometry is shown schematically in Fig. 1B, as well as TEM micrographs of the domain structure before and after switching by a 4 V dc bias, which exceeds the threshold switching voltage (V_c) for this region. A ~270 nm-wide $P_{[11\bar{1}]P}$ domain formed from the initial $P_{[111]P}$ state, corresponding to the same 71° switching path observed in the full film. The polarization direction was determined from the cation positions, using high-resolution scanning TEM (STEM) in high-angle annular dark field (HAADF) mode (*20*, *21*) (fig. S3).

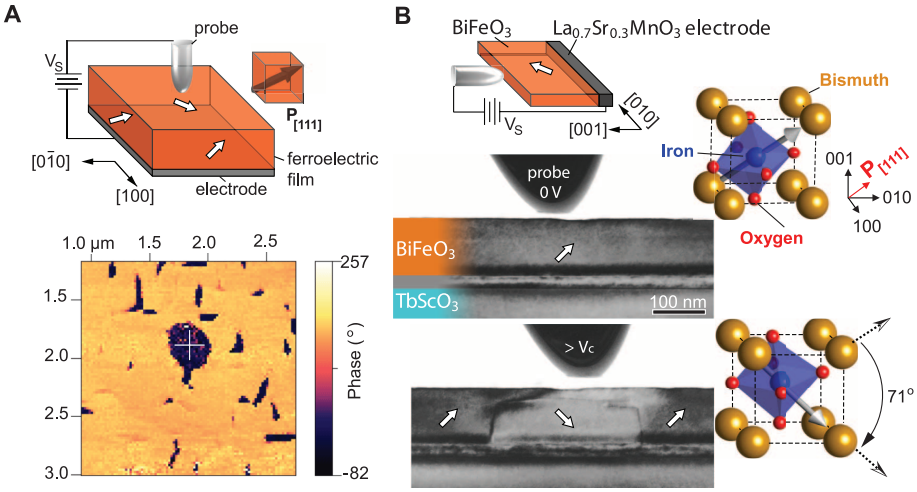

Fig. 1. Thin-film ferroelectric switching by a surface probe. (**A**) An out-of-plane PFM phase image shows the reversed downward-poled domain formed by application of a 20.6-V bias to a probe on the surface of the 100-nm $BiFeO_3$ film. (**B**) A thin cross-sectional TEM image of the same film before and after switching by a 4-V bias. Switching occurs by 71° rotation of the polarization beneath the tungsten tip.

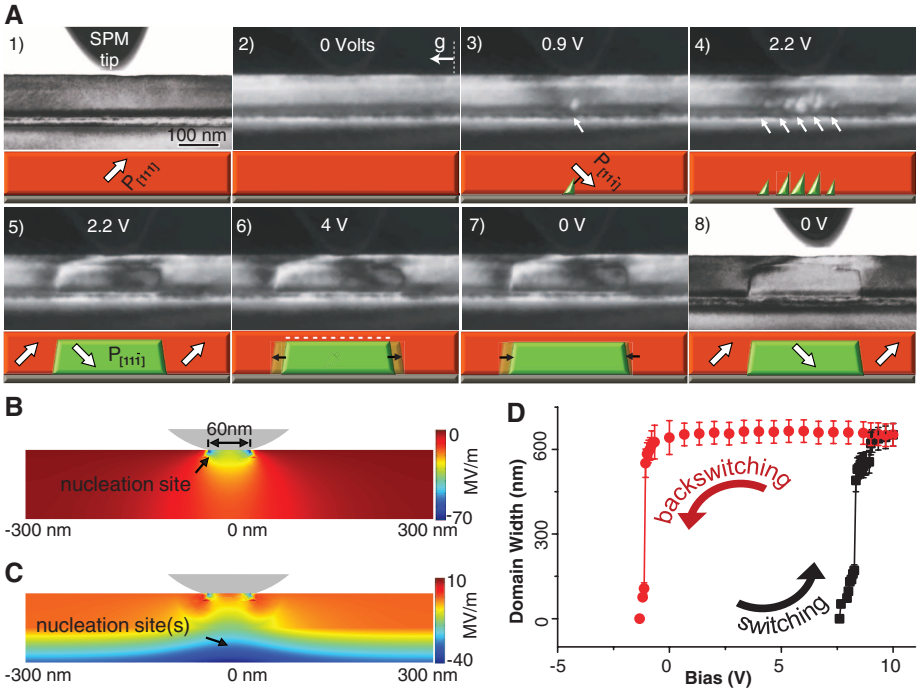

Fig. 2. (**A**) A chronological TEM dark-field image series formed by using the reflection $g = 040_P$ depicts the evolution of a $P_{[11\bar{1}]P}$ domain from a single-domain $P_{[111]P}$ film. Nucleation occurs at the $La_{0.7}Sr_{0.3}MnO_3$ electrode interface at 0.9 V (images 1 to 3), producing a metastable stationary domain. Additional bias increases the size and number of these domains up to 2.2 V (image 4). At 2.2 V, the domains merge and propagate forward just short of the surface (image 5), where they remain pinned along a $(001)_P$ plane even after the voltage is nearly doubled (image 6). The lateral extent of the domain is reduced slightly with the removal of the bias (image 7) and remains unchanged after the tip is removed (image 8). (**B**) Normal component of the electric field from the surface probe. (**C**) Normal component of the electric field, including top and bottom Schottky junctions. (**D**) A ferroelectric hysteresis loop formed by the primary 71° switching as determined by the area of a switched domain.

The nucleation of ferroelectric domains occurs when the applied field exceeds a critical nucleation threshold (the coercive field), which is subject to regional variation from defects (*22*). The interface is the expected nucleation site because of its high free energy due to the broken symmetry, strain, electric fields, charge, and altered chemical structure, which decrease the nucleation barrier (*16*). The high field concentration formed at the tip of the surface probe is generally assumed to dominate over any built-in electric fields, such as from Schottky junctions, and to initiate switching at the free surface, where the applied field is highest. However, a chronological series of TEM micrographs in Fig. 2 of 71° $P_{[111]P}$ to $P_{[11\bar{1}]P}$ switching during a slow ramp of the dc probe bias from 0 to 4 V clearly shows multiple nucleation events occurring exclusively at the bottom interface (movie S2). The out-of-plane electric field, E_Z, for this tip geometry at 2-V bias calculated by finite element analysis (Fig. 2B), is concentrated at the free surface. Hall measurements performed on nonbuffered 100-nm $BiFeO_3$ films showed an n-type conductivity. Inclusion of built-in electric fields from Schottky barriers of 0.85 and 0.77 V from junctions of n-type $BiFeO_3$, with $La_{0.7}Sr_{0.3}MnO_3$ and tungsten, respectively (*23*), produces the total E_Z field distributions shown in Fig. 2C. There is a broad band along the $La_{0.7}Sr_{0.3}Mn0_3$ interface where $P_{[11\bar{1}]P}$ nucleation is likely to occur because of a strong negative field (pointed toward the substrate), which is in agreement with TEM observations. The electrical properties of the Schottky junctions could not be probed because conduction was bulk-limited (fig. S4); however, they are a common feature of planar ferroelectric oxides (*16*, *24*) and are known to determine nucleation sites between symmetric planar electrodes in $BiFeO_3$ films (*18*). The relative strengths and distributions of the built-in fields vary, given assumptions about the Schottky barrier heights, the depletion width, and the electrode geometry. Regardless, the built-in fields shown in Fig. 2 are of the same order of magnitude as the tip field and cannot be neglected.

The triangular domains that nucleated at the $La_{0.7}Sr_{0.3}MnO_3$ interface were metastable, increasing (compare Fig. 2A, images 3 and 4) or decreasing their fixed size with the applied bias. Multiple nucleation events occured before a critical voltage of 2.2 V, whereupon they coalesced and expanded into a single domain that reached its full forward extent within a single 30-ms data sample. The triangular shape of these domains served to minimize depolarizing fields as the domain walls oriented closer to charge-neutral $(011)_P$ planes. During this low field stage of thermodynamically limited switching, nuclei extended

Downloaded from www.sciencemag.org on November 17, 2011

~200 nm laterally across the interface, over three times the contact area of the tip. Such delocalization of switching under a localized field may be an important consideration for surface probe measurements. More fundamentally, this process is a departure from the kinetically limited models used to describe ferroelectric switching (*24*). This is important for electrical characterization, because the switching transient does not necessarily correspond to the actual nucleation bias.

The metastable behavior indicates an intrinsic thermodynamic instability of the nuclei such as from positive built-in fields or an accumulation of strain, which destabilize the domain away from the interface. We do not see this behavior in similar nonferroelastic 180° switching of tetragonal $PbZr_{0.2}Ti_{0.8}O_3$ films, which suggests that strain from ferroelastic 71° switching is a contributing factor. Hysteresis loops measuring the switched domain area during cyclic switching under the probe have a positive voltage offset, indicating a possible positive built-in field (Fig. 2D). The reduction of this offset during cycling (fig. S5) further suggests that it may be the result of polar defects "imprinted" to the original $P_{[111]P}$ polarization (*25*), which disassociate during cycling. A contribution to the offset is also expected because of dissimilar electrode thermal histories and work functions [4.8 eV for $La_{0.7}Sr_{0.3}MnO_3$ (*26*) versus ~4.5 eV for polycrystalline tungsten

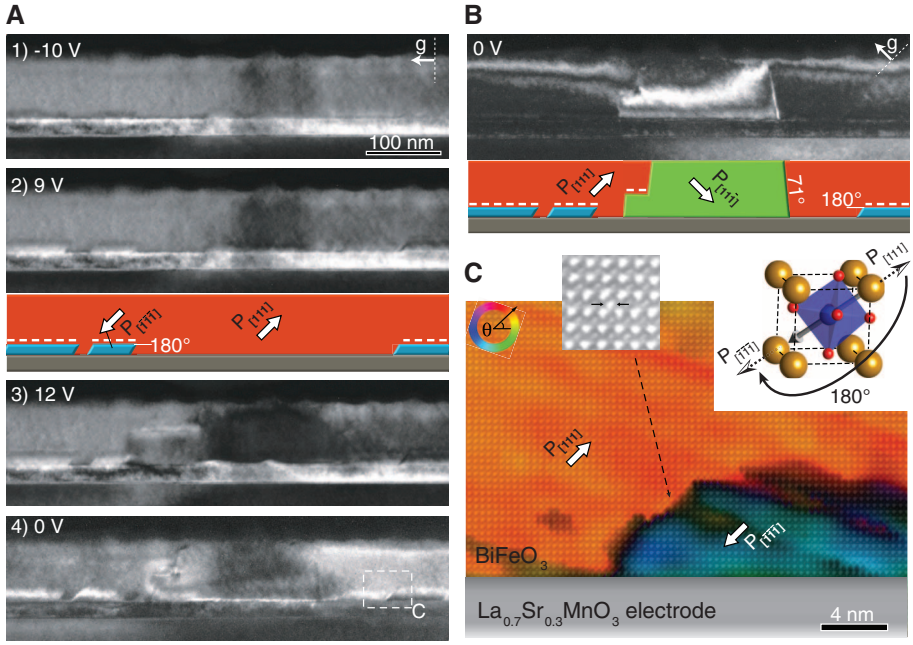

Fig. 3. Near-interface switching. (**A**) A chronological TEM image series of the $P_{[111]P}$ $BiFeO_3$ cross-section as the voltage increases from −10 V to +12 V (images 1 to 3) and back to zero (image 4) formed from $g = 040_P$ diffraction of the vertical planes and (**B**) $g = 0\bar{4}4_P$ diffraction of inclined planes. 180°-rotated $P_{[\bar{1}\bar{1}\bar{1}]P}$ interfacial domains and a 71°-rotated $P_{[11\bar{1}]P}$ primary domain appear sequentially, shown by the accompanied schematics. (**C**) A high-resolution HAADF image shows the polarization distribution at the edge of an interfacial domain, where the color and its intensity correspond to polarization angle and magnitude, respectively. The inset HAADF image shows an example of a point defect located at the domain wall.

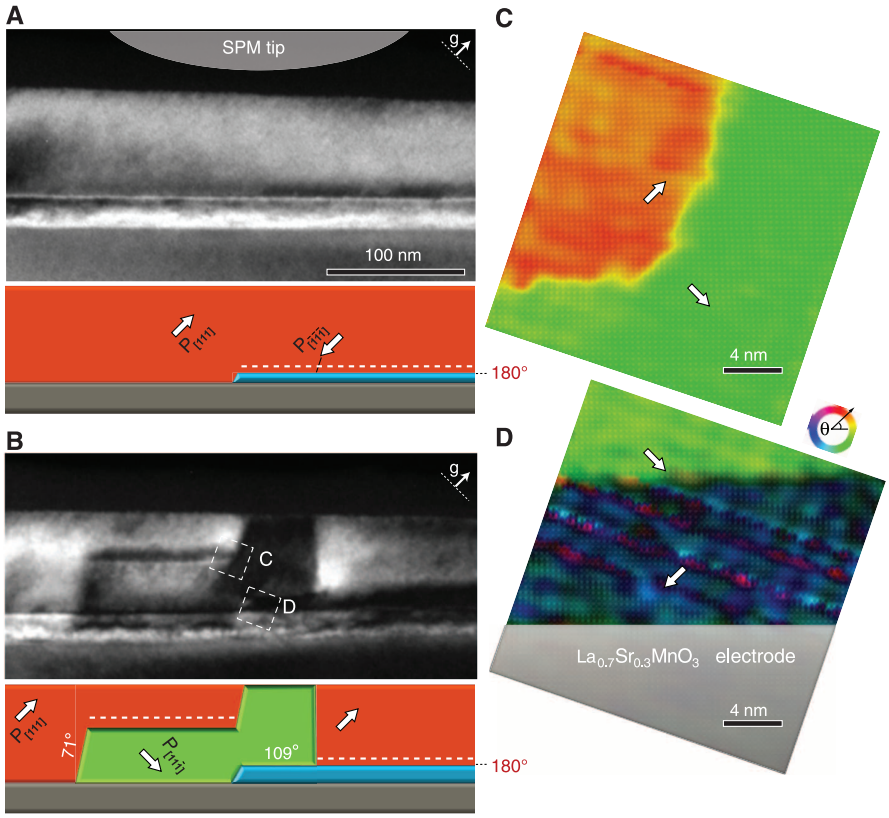

Fig. 4. Polarization mapping of coincident 71° and 180° switching. A region of a $P_{[111]P}$ $BiFeO_3$ film is switched in the vicinity of a 180° $P_{[\bar{1}\bar{1}\bar{1}]P}$ interfacial domain. (**A**) The interfacial domain appears as a dark band on the right half of the dark-field TEM image, $g = 044_P$, as shown in the corresponding diagram. (**B**) A $P_{[11\bar{1}]P}$ domain formed by subsequent switching of this region, with the left side pinned mid-film producing a negatively charged domain wall. Polarization maps from the highlighted regions show there is (**C**) a single $P_{[11\bar{1}]P}$ polarization at the pinning boundary and that (**D**) the $P_{[\bar{1}\bar{1}\bar{1}]P}$ domain remains at the interface.

Downloaded from www.sciencemag.org on November 17, 2011

(*27*)], but these favor a dominance of the negative-field Schottky junction, which would produce a negative shift. An alternate contribution to this offset may stem from the positive-voltage branch switching by a nucleation event, and the subsequent negative-voltage branch backswitching by the shrinking of the switched domain (fig. S6 and movie S3). The critical field for nucleation and the threshold field for the onset of domain wall creep need not be the same.

A 71° polarization reversal accounts for the majority of the area beneath the probe. However, this "primary" domain often does not extend the full width between the two electrodes. Despite the high-energy domain wall that is created, the forward-propagating domain is often pinned midway through the film, leaving the top layer unswitched as shown in Fig. 2A. Furthermore, a thin layer of film along the $La_{0.7}Sr_{0.3}MnO_3$ buffer electrode layer undergoes an independent switching process from the primary domain. A chronological TEM image series in Fig. 3A shows the domain structure evolution as the film is biased from –10 to 20 V and back to zero. At a small positive bias, long horizontal domains confined to the interface appear (Fig. 3A, image 2, and movie S4) and increase in height with increasing bias. Ultimately, a primary 71° switched $P_{[11\bar{1}]_P}$ domain forms directly beneath the tip (Fig. 3A, image 3). Both the interfacial and primary domains persist after the bias is removed (Fig. 3A, image 4). Dark-field images formed from reflections of the $(011)_P$ planes (Fig. 3B) indicate that the interfacial domains (invisible in the image) do not form the same ferroelastic twin with the unswitched region as the primary domain (bright area). Polarization mapping from HAADF images confirms that the interfacial domains undergo a nonferroelastic 180° polarization rotation (Fig. 3C). The switching thresholds of the interfacial domains have a large negative-voltage offset as compared to the primary domain. They have a lower nucleation bias and form several hundred nanometers away from the tip. In contrast, they require much larger negative voltages to erase (movie S5) because of the need to overcome the negative field in the Schottky junction where they are located.

The lateral edges of the interfacial domains are charge-neutral $(011)_P$ 180° domain walls. However, the nominally $(001)_P$ horizontal domain wall is unfavorable because of its negative charge from the tail-to-tail polarization vectors. Its graded appearance indicates that it is not a sharp $(001)_P$ boundary, but is inclined or corrugated to reduce the depolarizing field. Despite the energy cost of this domain wall, the interfacial domains exhibit long-term stability (>6 months and ongoing). Although the interfacial domains and primary switched domain do not overlap in Fig. 3A, Fig. 4 shows a region with an interfacial domain directly beneath the tip before switching (Fig. 4A). The subsequent formation of the primary 71° domain does not consume or otherwise alter the interfacial domain except to create a sharper $(001)_P$ domain wall, because the domain wall charging is absent (Fig. 4B).

Although the vertical extent of the interfacial domains depends on the voltage history, the lateral edges are fixed. HAADF images of the inclined 180° domain walls show a high density of point defects, such as the heavy-element substitution in the Fe site shown in the insert in Fig. 3C, as well as defects in the oxygen site (fig. S7). The interaction of the domain walls with the point defects is likely to be strain-mediated because the domain walls are neutrally charged. This is not the case for the negatively charged horizontal domain walls created by pinning of the 71° domain, such as the shoulder on the left sides of Figs. 3A and 4B and the entire switched region in Fig. 2A. The pinning behavior points to ordered planes of charged defects as the active pinning site. Vacancies and defect dipoles are common in perovskite films (*25*, *28*), especially those grown by molecular beam epitaxy (*29*). Furthermore, the pinning occurs at fixed inhomogeneously distributed sites, which are repeatable for any given region of the film (fig. S8 and movie S6). We could not see any structural defects associated with the pinning sites, any detectable thickness variation in a thickness map of the pinned region (fig. S1), or any systematic steps along the $(001)_P$ planes in a topographic atomic force microscopy scan of the ion-etched surface of a prepared TEM sample. The pinning barrier can be overcome with the application of a sufficiently large bias or by repositioning the probe (movie S7), confirming that the film is still ferroelectric and the switched domain is thermodynamically stable beyond the pinning site. Although the oxygen-scattering cross-section is too small for the oxygen site to be seen directly in the HAADF images, these results strongly support the theory of domain pinning by ordered planes of oxygen vacancies (*30*).

The observed ferroelectric switching, although it may manifest in some applications as a 71° single-domain switching process, is found to be more complex than is conventionally assumed. In particular, reversible switching at the interfaces is impeded, which is of particular consequence for heterostructures dependent on the ferroelectric interface state, such as the $BiFeO_3/La_{0.7}Sr_{0.3}MnO_3$ film stack studied here. Film orientations that favor single strain-free switching paths such as $(001)_P$ tetragonal or $(111)_P$ rhombohedral ferroelectrics can avoid some of this complexity, but this is not possible for heterostructures such as this one, which require ferroelastic switching (*31*). We have also found that substantial contributions by built-in electric fields lead to a large delocalization of switching from the tip, especially the formation of interfacial domains. The energetics favoring the nucleation and growth of 71° domains despite the presence of favorably oriented yet oddly immobile preexisting 180° domains is unknown. Future studies on the interface structure and its effect on switching or the inclusion of additional electrostatic contributions such as from inhomogeneous space charges, depolarizing fields from finite screening, and flexoelectric effects may help elucidate this behavior.

References and Notes

1. J. F. Scott, C. A. Paz de Araujo, *Science* **246**, 1400 (1989).
2. J. F. Scott, *Science* **315**, 954 (2007).
3. V. Garcia *et al.*, *Nature* **460**, 81 (2009).
4. K. Aizu, *J. Phys. Soc. Jpn.* **27**, 387 (1969).
5. F. Kubel, H. Schmid, *Acta Crystallogr. Sect. B Struct. Commun.* **46**, 698 (1990).
6. Y. H. Chu *et al.*, *Nat. Mater.* **7**, 478 (2008).
7. P. Maksymovych *et al.*, *Science* **324**, 1421 (2009).
8. S. M. Wu *et al.*, *Nat. Mater.* **9**, 756 (2010).
9. W. J. Merz, *Phys. Rev.* **95**, 690 (1954).
10. T. Tybell, P. Paruch, T. Giamarchi, J. M. Triscone, *Phys. Rev. Lett.* **89**, 097601 (2002).
11. Y. H. Shin, I. Grinberg, I. W. Chen, A. M. Rappe, *Nature* **449**, 881 (2007).
12. A. Kuroda, S. Kurimura, Y. Uesu, *Appl. Phys. Lett.* **69**, 1565 (1996).
13. V. Gopalan, T. E. Mitchell, *J. Appl. Phys.* **83**, 941 (1998).
14. M. P. Cruz *et al.*, *Phys. Rev. Lett.* **99**, 217601 (2007).
15. M. W. Chu *et al.*, *Nat. Mater.* **3**, 87 (2004).
16. A. K. Tagantsev, G. Gerra, *J. Appl. Phys.* **100**, 051607 (2006).
17. D. Pantel *et al.*, *J. Appl. Phys.* **107**, 084111 (2010).
18. N. Balke *et al.*, *Adv. Funct. Mater.* **20**, 3466 (2010).
19. S. H. Baek *et al.*, *Nat. Mater.* **9**, 309 (2010).
20. C. L. Jia *et al.*, *Nat. Mater.* **6**, 64 (2007).
21. C. T. Nelson *et al.*, *Nano Lett.* **11**, 828 (2011).
22. S. Jesse *et al.*, *Nat. Mater.* **7**, 209 (2008).
23. S. J. Clark, J. Robertson, *Appl. Phys. Lett.* **90**, 132903 (2007).
24. M. Dawber, K. M. Rabe, J. F. Scott, *Rev. Mod. Phys.* **77**, 1083 (2005).
25. C. M. Folkman *et al.*, *Appl. Phys. Lett.* **96**, 052903 (2010).
26. M. P. de Jong, V. A. Dediu, C. Taliani, W. R. Salaneck, *J. Appl. Phys.* **94**, 7292 (2003).
27. E. W. Müller, *J. Appl. Phys.* **26**, 732 (1955).
28. G. L. Yuan, A. Uedono, *Appl. Phys. Lett.* **94**, 132905 (2009).
29. J. Zhang *et al.*, *J. Vac. Sci. Technol. B* **27**, 2012 (2009).
30. J. F. Scott, M. Dawber, *Appl. Phys. Lett.* **76**, 3801 (2000).
31. T. Zhao *et al.*, *Nat. Mater.* **5**, 823 (2006).

Acknowledgments: This work was supported by the U.S. Department of Energy (DOE), Office of Basic Energy Sciences, Division of Materials Sciences and Engineering, under award DE-FG02-07ER46416 and partially by NSF under awards DMR-0907191 (P.G. and K.Z.), DMR-0820404 (J.R.J.), and DMR-0723032 (aberration-corrected TEM instrument); at Cornell University by Army Research Office (ARO) grant W911NF-08-2-0032; at Penn State University by the U.S. Department of Energy under award DE-FG02-07ER46417; at the University of Wisconsin–Madison by ARO grant W911NF-10-1-0362; and at the University of Washington by ARO grant W911NF-07-1-0410. The authors also acknowledge the National Center for Electron Microscopy at Lawrence Berkeley National Laboratory for their support under the DOE grant DE-AC02-05CH11231 for user facilities. The project was conceived and directed by X.Q.P.; C.T.N., D.G.S., and X.Q.P. wrote the manuscript; TEM experiments were performed and analyzed by C.T.N. and P.G. under the guidance of X.Q.P.; $BiFeO_3$ and $La_{0.7}Sr_{0.3}MnO_3$ films were fabricated using molecular beam epitaxy by C.H., C.A., and A.M. under the guidance of D.G.S.; PFM experiments were performed by J.R.J. and Y.M.L. under the supervision of J.Y.L.; Hall measurements were performed by K.Z. under the supervision of X.Q.P.; sputtered films were grown by C.M.F. and S.H.B. under the supervision of C.B.E.; phase-field simulations were carried out by B.W. and Y.J.G. under the supervision of L.Q.C.; and E.G.W. participated in the modeling and analysis of interfacial properties.

Supporting Online Material

www.sciencemag.org/cgi/content/full/334/6058/968/DC1
Materials and Methods
Figs. S1 to S8
References (*32*–*34*)
Movies S1 to S7

14 April 2011; accepted 12 October 2011
10.1126/science.1206980

Downloaded from www.sciencemag.org on November 17, 2011